Atmospheric Environment 43 (2009) 879–888

Contents lists available at ScienceDirect

Atmospheric Environment

journal homepage: www.elsevier.com/locate/atmosenv

Optical and microphysical properties of severe haze and smoke aerosol measured by integrated remote sensing techniques in Gwangju, Korea

Young M. Noh [a], Detlef Müller [a,b], Dong H. Shin [a], Hanlim Lee [a], Jin S. Jung [a], Kwon H. Lee [c], Maureen Cribb [c], Zhanqing Li [c], Young J. Kim [a,*]

[a] Advanced Environmental Monitoring Research Center (ADEMRC), Department of Environmental Science & Engineering, Gwangju Institute of Science and Technology (GIST), 1 Oryong-dong, Buk-gu, Gwangju 500 712, Republic of Korea
[b] Leibniz Institute for Tropospheric Research (IfT), Germany
[c] Earth System Science Interdisciplinary Center (ESSIC), Department of Atmospheric & Oceanic Science, University of Maryland (UMD), College Park, MD 20742, USA

ARTICLE INFO

Article history:
Received 9 July 2008
Received in revised form
17 October 2008
Accepted 21 October 2008

Keywords:
Haze
Raman lidar
Satellite
Single-scattering albedo

ABSTRACT

Aerosol optical and microphysical parameters from severe haze events observed in October 2005 at Gwangju, Korea (35.10°N, 126.53°E) were determined from the ground using a multi-wavelength Raman lidar, a sunphotometer, and a real-time carbon particle analyzer and from space using satellite retrievals. Two different aerosol types were identified based on the variability of optical characteristics for different air mass conditions. Retrievals of microphysical properties of the haze from the Raman lidar indicated distinct light-absorbing characteristics for different haze aerosols originating from eastern and northern China (haze) and eastern Siberia (forest-fire smoke). The haze transported from the west showed moderately higher absorbing characteristics (SSA = 0.90 ± 0.03, 532 nm) than from the northern direction (SSA = 0.96 ± 0.02). The organic/elemental carbon (OC/EC) ratio varied between 2.5 ± 0.4 and 4.1 ± 0.7.

1. Introduction

East Asia is one of the major source regions in the world of anthropogenic aerosols originating from fossil fuel combustion and natural aerosols such as mineral dust. Smoke from forest fires in Siberia is an additional source of aerosols in East Asia (Lee et al., 2005). Due to the combined effect of the expansion of arid dust-producing regions, increasing regional populations, and increasing fossil fuel usage in China, the aerosol burden in the region is expected to continuously increase into the future (Luo et al., 2001; Lee et al., 2006a,b). Korea is located in the downwind area of the Asian continent and is often affected by long-range transported aerosols such as Asian dust, forest-fire smoke, and anthropogenic aerosols under westerly wind conditions (Chun et al., 2001; Park and Kim, 2004; Ryu et al., 2004; Lee et al., 2006a,b). Determination of the optical and microphysical properties of various atmospheric aerosols transported to the Korean peninsula is important in order to estimate their effects on air quality and climate change in the region. A number of studies focusing on transport characteristics as well as optical and chemical properties of Asian dust particles have been conducted (Huebert et al., 2003; Murayama et al., 2003; Arimoto et al., 2006). For aerosol monitoring in East Asia, satellite data can provide useful information on the spatial and temporal distributions of atmospheric aerosols (Lee et al., 2006a,b, 2007). Ground-based measurements of particulate matter (PM) give continuous information about its optical and physical characteristics (Kim et al., 2004; Kim, 2007).

Information on the vertical distribution of aerosols is important for understanding its transport characteristics as well as its radiative effect. The Raman lidar can directly measure vertical profiles of the particle extinction coefficient without assuming a lidar ratio, unlike so-called elastic lidars. Raman lidars have been used to measure vertical profiles of tropospheric aerosol optical properties in different parts of the world (Wandinger et al., 1995; Ansmann et al., 2000; Müller et al., 2000b, 2003; Ferrare et al., 2001; Matthias et al., 2004). For example, Murayama et al. (2004) investigated optical and microphysical properties of Siberian forest-fire smoke plumes in the free troposphere using a multi-wavelength Raman lidar in Tokyo, Japan. Noh et al. (2007, 2008) studied the lidar ratio characteristics of various aerosols using a Raman lidar in Korea. Although some Raman lidar measurements from a few select locations in Asia exist, there is still a dearth of such measurements concerning aerosol optical and microphysical properties in East Asia.

The main objective of this paper is to investigate the optical and microphysical characteristics of atmospheric aerosols

* Corresponding author. Tel.: +82 62 970 3401; fax: +82 62 970 3404.
E-mail address: yjkim@gist.ac.kr (Y.J. Kim).

1352-2310/$ – see front matter © 2008 Elsevier Ltd. All rights reserved.
doi:10.1016/j.atmosenv.2008.10.058

observed under severe haze conditions during October 2005 in Gwangju, Korea. Integrated monitoring of atmospheric aerosols using a multi-wavelength Raman lidar, satellite retrievals, a sunphotometer, and a real-time carbon particle analyzer was performed. In this study, satellite data were used to track the haze plume and to determine its aerosol optical depth over the northeast-Asian region. Sunphotometer data were used to detect temporal variations in aerosol optical depth (AOD) during the observation periods. In addition to the vertical distribution, optical and microphysical properties of the haze plume were also retrieved from an inversion algorithm using the multi-wavelength Raman lidar data. Continuous real-time measurements of organic and elemental carbon (OC and EC) concentrations were also made to characterize the differences in the aerosol chemistry of the observed haze particles.

2. Measurements

Integrated monitoring of atmospheric aerosols was performed at the campus of the Gwangju Institute of Science & Technology (GIST) located in Gwangju, Korea (35.10°N, 126.53°E) from 15 to 28 October 2005. The GIST multi-wavelength Raman lidar system (Noh et al., 2007) was used to measure vertically resolved particle backscatter coefficients, extinction coefficients, and extinction-to-backscatter (lidar) ratios based on the methodology described by Ansmann et al. (1990, 1992). Particle extinction coefficients can be retrieved by the GIST Raman lidar system above 780 m and 540 m at measurement wavelengths of 355 nm and 532 nm, respectively. Overlap functions were retrieved using the method described by Wandinger and Ansmann (2002). Extinction profiles at 355 and 532 nm were derived from the nitrogen Raman signals. Sliding average of 360-m length below 2400 m altitude and 600-m length above 2400 m altitude were applied to the range-corrected nitrogen Raman signals. Detailed descriptions of signal summation and averaging length are presented by Noh et al. (2007, 2008). The effect of incomplete overlap between the outgoing laser beams and the receiver telescopes is canceled out for profiles of the backscatter coefficients because the ratio of two signals, elastic backscattering from particles and molecules and the nitrogen Raman signals, is taken (Ansmann et al., 1992). Thus the backscatter coefficient measurement is reliable down to 120 m altitude for the lidar system used in this study. Backscatter coefficient at 1064 nm was calibrated using size-independent backscattering characteristics of high altitude ice-crystal cloud between 532 and 1064 nm wavelengths. The uncertainty of measurement less than 10% was obtained for 1064 nm backscattering coefficient by calibration. The statistical errors of the retrieved extinction and backscatter coefficients were estimated to be <10–20% and <5–10%, respectively.

Lidar-derived total column aerosol optical depth (AOD) was calculated by integrating the profile of the extinction coefficient from the ground up to the 6-km altitude. Above that height the signal-to-noise ratio was too low for an accurate determination of particle extinction coefficients. Particle extinction coefficients below the height of full overlap, i.e. between 780 m and 120 m, were derived from the measured backscattering coefficient using the average lidar-ratio value estimated for the boundary layer. The lidar ratio was assumed constant within the planetary boundary layer. Extinction coefficient at the ground was assumed to invariant below 120 m height. Microphysical parameters such as particle effective radius, volume and surface-area concentration, and complex refractive index can be derived by through use of an inversion algorithm (Müller et al., 1999a,b, 2000a). Particle backscatter coefficients at the three laser wavelengths and particle extinction coefficients at 355 and 532 nm were used as input data for the inversion algorithm. The particle single-scattering albedo (SSA) at 532 nm was calculated using a Mie-scattering algorithm (Bohren and Huffman, 1983). The volume concentration distribution and the mean (wavelength-independent) complex refractive index are retrieved with the inversion algorithm (Müller et al., 1999a). The volume concentration distribution is determined from Eq. (1),

$$g_i(\lambda) = \int_{r_{\min}}^{r_{\max}} K_i(r, m, \lambda, s)\frac{3}{4r}v(r)\,\mathrm{d}r, \quad g_i = \alpha, \beta \tag{1}$$

where $g_i(\lambda)$ denotes the extinction coefficient α or the backscatter coefficient β at wavelength λ, $v(r)$ describes the volume concentration of particles per radius interval dr, and $K_i(r, m, \lambda, s)$ is the kernel efficiency of extinction or backscattering for single particles. The efficiencies depend on the radius r of the particles, on their complex refractive index m, on the wavelength λ of the interacting light, and on the shape s of the particles.

We solve this equation on the basis of inversion with regularization. We use base function approximate the investigated particle size distributions. The base functions are *B*-splines of first order, i.e. they have a triangular shape on a semi-logarithmic scale. The numerical solution of equation (1) provides weight factors which are needed to derive the size distribution with the base functions. In the solution process, the constraint of smoothness of the retrieved volume concentration distribution serves as a regularization parameter for stabilizing the inverse problem (Müller et al., 1999a,b). The degree of this regularization is determined with the modified minimum discrepancy principle (Veselovskii et al., 2002). Four-hundred inversion windows of variable width are defined through variation of the lower and upper limits of the base function range: from 0.01 to 0.2 μm ($r_{\min}$) and from 1 to 10 μm ($r_{\max}$), respectively. The base functions are distributed logarithmically equidistant within the inversion windows (Müller et al., 1999a,b). The inversion is performed for every window and for a grid of wavelength- and size-independent complex refractive indices that vary from 1.33 to 1.8 in real and from 0 to 0.1 in imaginary part.

In the final step, from the individual inversion solutions only those are selected, for which the back-calculated optical data agree with the original data within the limits of the measurement error. The mean particle size in terms of the effective radius and integral particle parameters, i.e. the total volume, surface-area, and number concentrations, are calculated from the selected solutions, and their mean values and standard deviations are presented as final inversion results. In this way, one also obtains a range of complex refractive indices.

The single-scattering albedo is then calculated from the volume concentration distribution and the mean complex refractive index. Extended simulation studies (Veselovskii et al., 2002) show that an appropriate reconstruction of the volume distribution and mean complex refractive index is found from the five optical data (backscatter coefficient at 355, 532, 1064 nm and extinction coefficient at 355 and 532 nm) derived with our lidar system. Error analysis for the inversion results was discussed in detail by Müller et al. (1999a,b) and Veselovskii et al. (2002). An error analysis, which followed from simulations with synthetic as well as experimental data, showed that for realistic measurement errors of 20% the effective radius may be retrieved with an accuracy of 20–30%, volume and surface-area concentration with an accuracy of 50%. With respect to the complex refractive index its real part deviated by less than ±0.05, and its imaginary part by less than ±50%, from the correct value (Müller et al., 1999a).

During the periods of the lidar observations, physical, chemical and optical properties of aerosols were also measured with in-situ instruments at the surface. The hygroscopic growth factor (f(RH)),

defined as the light scattering coefficient of humidified aerosols divided by that of dry aerosols, was determined from the following equation:

$$f(\mathrm{RH})\_\mathrm{measured} = \frac{b_{\mathrm{scat}}(\mathrm{RH})}{b_{\mathrm{scat}}(\mathrm{dry\ PM_{2.5}}) + 0.3[\mathrm{CM}]}$$

where $b_{\mathrm{scat}}(\mathrm{RH})$ is the aerosol light scattering coefficient measured by an open chamber nephelometer at ambient humidity level, $b_{\mathrm{scat}}(\mathrm{dry\ PM_{2.5}})$ represents the dry $PM_{2.5}$ aerosol light scattering coefficient measured by a size-cut nephelometer, and [CM] is the coarse mass. For comparison with ambient b_{scat}, the CM dry mass scattering efficiency of 0.3 $m^2\,g^{-1}$ is used here, which is 50% lower than the Interagency Monitoring of Protected Visual Environments (IMPROVE, 2000) value of 0.6 $m^2\,g^{-1}$. This reflects the inability of the nephelometer to detect all of the light scattered forward by coarse particles (Molena, 1997; Ryan et al., 2005). Organic carbon (OC) and elemental carbon (EC) compositions of aerosol particles collected on quartz-fiber filters was measured with a Sunset Laboratory semi-continuous organic carbon/elemental carbon (OC/EC) analyzer using thermal-optical transmittance (TOT) protocol for pyrolysis correction (Kim et al., 2006a,b). The detailed sampling and analysis processes were described by Kim (2007).

Radiosonde observations conducted four times (03:00, 09:00, 15:00, 21:00 local time) a day by the Korean Meteorological Administration (KMA) at Gwangju airport located about 5-km away from the lidar observation site provided the vertical profiles of pressure, relative humidity and potential temperature. MODerate-resolution Imaging Spectro-radiometer (MODIS) satellite image was used to estimate the location and extent of haze plumes observed during the lidar observation period. The modified Bremen Aerosol Retrieval (BAER) method (von Hoyningen-Huene et al., 2003; Lee et al., 2005) was applied to MODIS Level-1 (L1) calibrated radiance data (collection 5) to retrieve the haze plume AODs. In this modified BAER, the seasonal minimum reflectance data were used in the surface reflectance determination (Lee et al., 2006a). Look up tables (LUTs) constructed by Santa Barbara Disort Atmospheric Radiative Transfer (SBDART) (Ricchiazzi et al., 1998) and aerosol optical properties from Aerosol Observation Network (AERONET) inversion products (Dubovik and King, 2000; Dubovik et al., 2002) were used to determine AOD from the aerosol reflectance. As the original version of BAER algorithm uses a spectral smoothing technique for the stability of multi-spectral dependent of AOD, this technique was also adopted to three visible bands (0.47, 0.55, 0.66 μm) of MODIS data acquired over land. The estimated error of MODIS aerosol retrieval used in this study was reported to be 12.5% (Lee et al., 2006b) and ±0.11 AOT (Lee et al., 2007). Quality-assured Level 2.0 sunphotometer data at the Gwangju AERONET site were used for comparing optical depths derived from the satellite and the lidar observations, respectively.

3. Results

3.1. Integrated monitoring of haze plume

Range-corrected, backscatter lidar signals acquired from the continuous measurement of aerosols from October 15 to 28, 2005 using an analog-to-digital converter (ADC) system (Noh et al., 2007) are shown in Fig. 1. No observations were made from October 21 to 24, 2005 due to precipitation and instrument problems. Fig. 1 shows that aerosols were mostly detected within the planetary boundary layer (1–2 km altitude) during the observation periods. Aerosol optical depths (AODs) at 440 nm were calculated from lidar-derived AOD at 532 nm and satellite-derived AOD at 550 nm using the Ångström exponent determined from lidar and sunphotometer data measurements, respectively. Daily-averaged AERONET AOD, satellite-derived AOD, and lidar-derived AOD at 440 nm are plotted in Fig. 2 to show the temporal variations of aerosol loading during the observation period. Lidar and sunphotometer data were not available on October 20, 21, 23, and 28 due to precipitation and cloud cover. Twelve-hour average values of surface PM_{10} concentrations obtained by a beta gauge during the daytime (07:00–19:00, local time) and the nighttime (19:00–07:00, local time) are also plotted in Fig. 2. Concentrations increased from October 15 until nighttime of October 17 and decreased during a precipitation event which lasted from the night of October 20 to October 21. Concentrations then increased rapidly to a maximum value of 159 μg m^{-3} on October 25th which corresponded to the date when the highest AOD value (2.28) was reached. AOD values retrieved by satellite during the daytime showed similar to or slightly higher values than those retrieved from the sunphotometer. Discrepancies between the two data sets must be resulted from the differences in spatial (satellite) and temporal (ground-based) dimensions. The variation in lidar-derived AOD retrieved during the nighttime showed a similar temporal trend to that of the surface measured PM_{10} concentration. It seems that most of the aerosols were detected within the planetary boundary layer (PBL).

Fig. 3 shows MODIS RGB (red, green, and blue) colour composite images of East Asia on October 17 and 24, 2005; they were created by mapping three MODIS visible bands centered at 660, 550, and 470 nm. A thick aerosol plume obscuring over East China and the Yellow Sea is seen in both images. Fig. 4 shows the MODIS-retrieved AOD at 550 nm obtained by the modified BAER algorithm (Lee et al., 2006a,b) for the lidar observation periods, i.e. October 15–19 and October 23–27, 2005. Areas where a cloud mask or sun-glint was

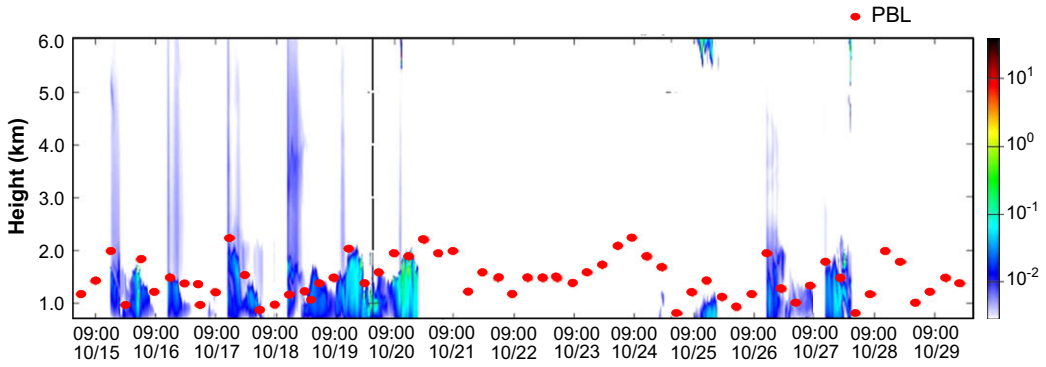

Fig. 1. Range-corrected backscattered signal at 532 nm recorded with the ADC system and planetary boundary layer (PBL) height measured by radiosonde (red spot) from October 15–28, 2005 at Gwangju, Korea. (For interpretation of the references to colour in this figure legend, the reader is referred to the web version of this article.)

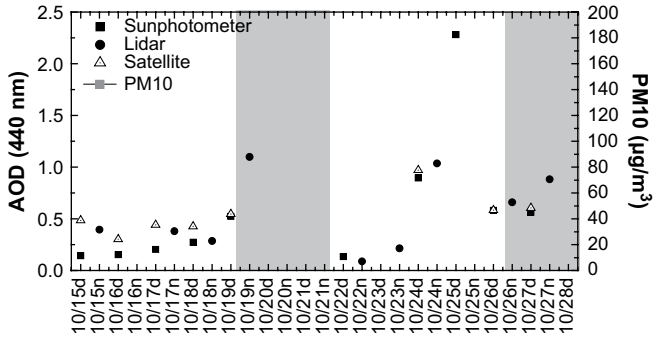

Fig. 2. Aerosol optical depth at 440 nm measured with a sunphotometer (daytime) and satellite (daytime), Raman lidar (nighttime) as well as the 12 h average surface PM_{10} concentration. Gray background color denotes the period that the smoke aerosol was detected. (For interpretation of the references to colour in this figure legend, the reader is referred to the web version of this article.)

present or areas where there was an orbital gap in the data are shown in white. High AOD values were consistently detected over East China during the observation period and the time series shows that haze aerosols were transported from East China to the Korean peninsula on October 17, 24, and 25, 2005. AOD values retrieved from satellite data above the lidar site generally assume similar to or higher values than the sunphotometer AOD values as seen in Fig. 2.

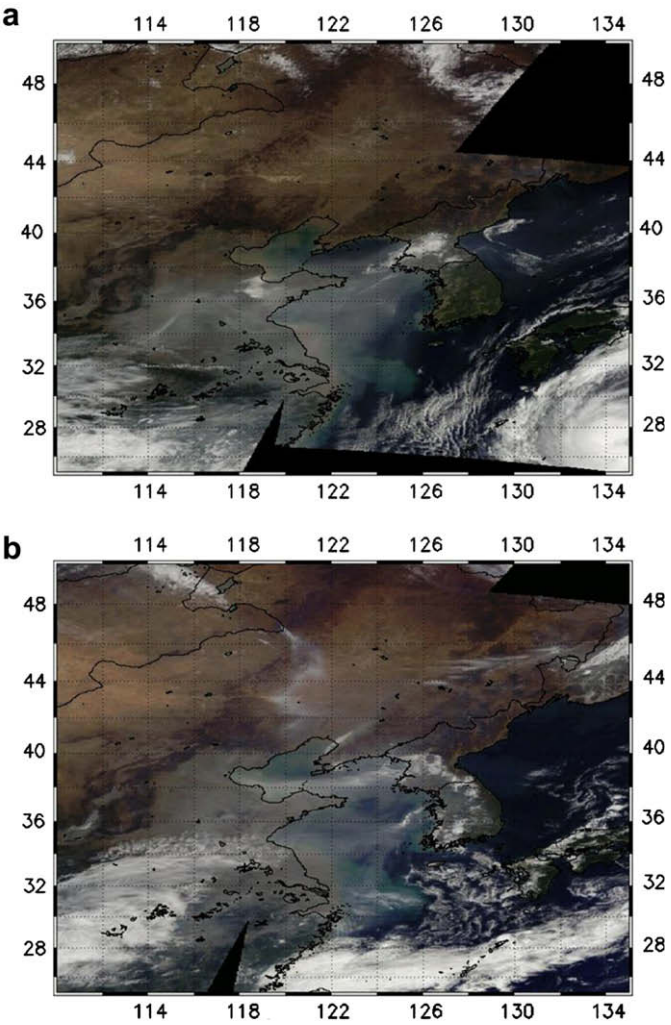

Fig. 3. MODIS RGB color composite image on (a) October 17 and (b) October 24, 2005. Note that the aerosol plume extends from East China to the Korean peninsula. (For interpretation of the references to colour in this figure legend, the reader is referred to the web version of this article.)

The NOAA/ARL Hybrid Single-Particle Lagrangian Integrated Trajectory model (HYSPLIT; Draxler and Rolph, 2003) was used to calculate the backward trajectories of air masses that reached the observation site (35.10°N, 126.53°E). The 5-day (120 h) backward trajectories of air masses at heights of 500, 1000, 2500 m were derived for 12:00 PM on each lidar observation day. HYSPLIT model calculation results for the arrival height of 2500 m (above PBL) show that on all observation days, the air mass was transported to the observation site from either the west or northwest region (East and Northeast China). However, the backward trajectory results for the arrival heights of 500 and 1000 m (within the PBL) show two different air mass movement patterns, as shown in Fig. 5. On most of the observation days, the air mass traveled from the northwest through East China to the observation site as shown in Fig. 5(a), resulting in the aerosol plume transport over the region of interest as shown in Fig. 4. On October 19, 26, and 27, 2005, air masses moved from the north through Siberia and north Korea to the observation site as shown in Fig. 5(b). Smoke aerosols due to forest fires in southeastern Siberia occasionally cause episodic air pollution events in East-Asian regions (Lee et al., 2005). Fig. 6 shows the accumulated fire spot counts obtained from the level 2 Terra/MODIS thermal anomalies/fire product (MOD14) (Kaufman et al., 1998) for the period of October 17–27, 2005. Although several fire spots were detected in the Northeast China region, most of the fire spots were detected in Northeastern Siberia. This strongly suggests that aerosols identified on October 19, 26, and 27, 2005 were affected by the transport of smoke aerosols originating from Siberia.

3.2. Optical and microphysical properties

Vertical profiles of extinction coefficients at 355 and 532 nm, backscatter coefficients at 355, 532 and 1064 nm, and lidar ratios, S_a at 355 and 532 nm acquired on October 24, 2005 are shown in Fig. 7(a–c). Lidar ratios below 780 m altitude denote average values estimated for the boundary layer in Fig. 7(c). The relative humidity and potential temperature profiles measured by radiosonde are included in Fig. 7(d). The slope of the relative humidity profile and the potential temperature profile were sharply changed around 1.5 km, which was identified as the top of the PBL located between 1.2 and 2.0 km. A haze plume was detected mostly within the PBL during the observation period as shown in Fig. 1.

Layer-averaged values of the aerosol optical properties only above 780 m because of the incomplete overlap were subsequently used for the inversion. Optical parameters from each aerosol layer such as lidar ratio at 355 and 532 nm, and Ångström exponent, Å as well as relative humidity, RH are summarized in Table 1. Each layer was categorized as consisting of either anthropogenic or smoke aerosols according to the air mass pathway patterns shown in Fig. 5. Air masses that moved from East and Northeast China were categorized as anthropogenic aerosols. Air masses that came from the eastern Siberia areas and north Korea were classified as smoke aerosols. Lidar-ratio values between the two types of air masses showed little difference, although the average value from anthropogenic aerosols is smaller than that of smoke aerosols as summarized in Table 1. Similar lidar-ratio values were obtained for anthropogenic aerosols at the two measurement wavelengths; 55.9 ± 2.5 sr and 58.2 ± 3.8 sr at 355 and 532 nm, respectively. For smoke aerosols, higher average lidar-ratio values were observed at 532 nm (62.9 ± 1.3 sr) than at 355 nm (55.8 ± 1.4 sr). To date, only limited lidar ratio observations of Asian aerosols are available for

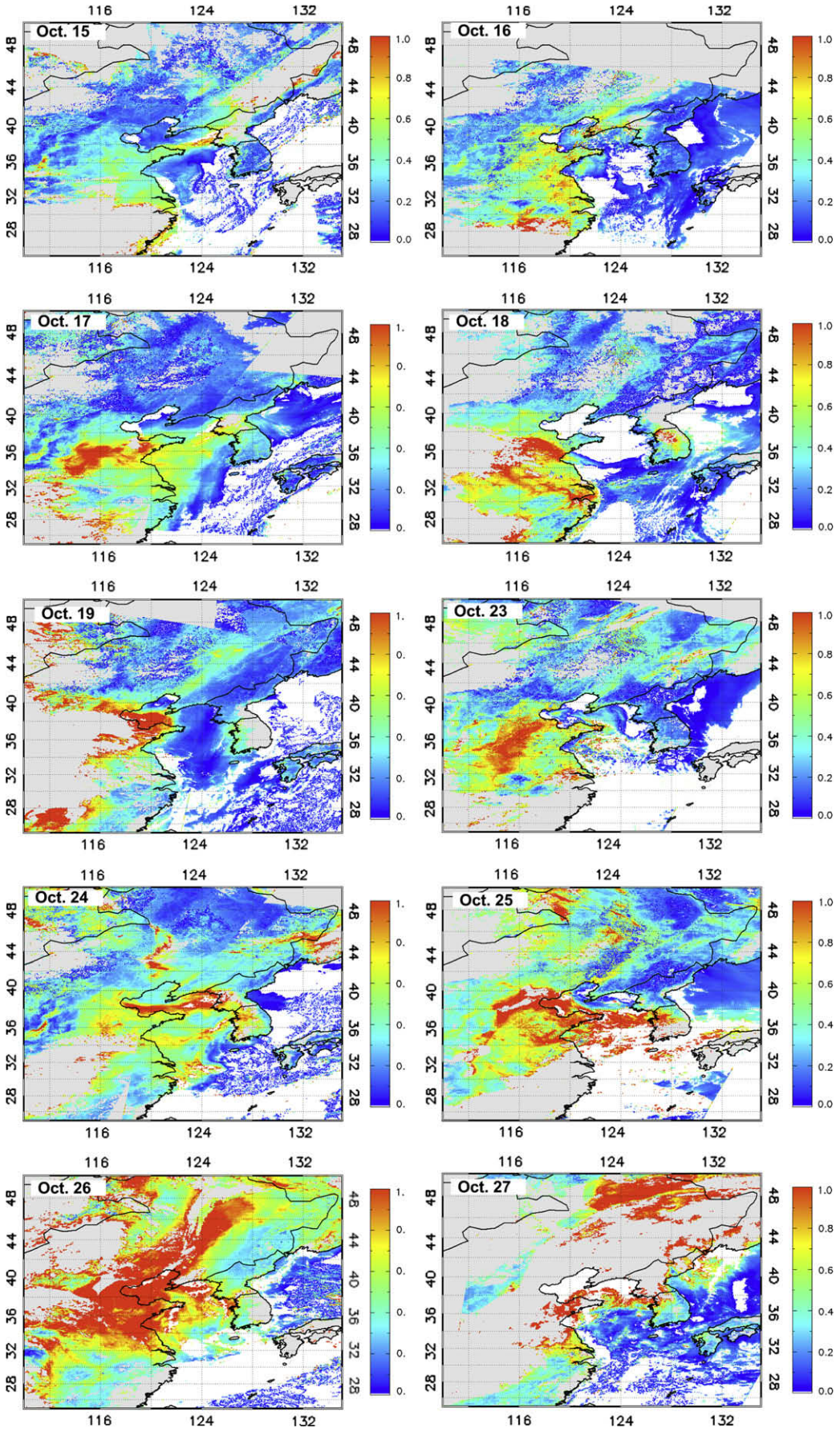

Fig. 4. MODIS-derived aerosol optical depth (AOD) observed at 2:00 PM during the haze event periods of October 15–19 and 23–27, 2005.

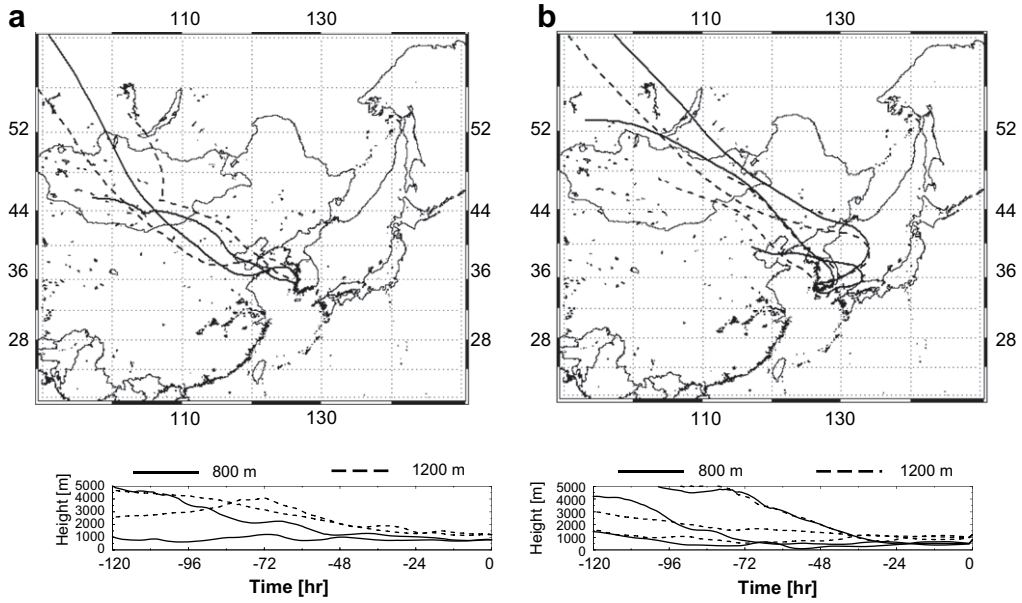

Fig. 5. Five-day HYSPLIT-4 backward trajectory analysis results. (a) Air masses moving in from the northwest direction on October 17 and 24, 2005. (b) Air masses transported from north and northeast directions on October 19, 26–27, 2005.

comparison purposes. Ansmann et al. (2005) and Tesche et al. (2007) obtained an average lidar ratio of 45.8 ± 5.6 sr at 532 nm from Raman lidar observations made at the Pearl River in southern China in October 2004. Cattrall et al. (2005) found a mean lidar ratio of 58 ± 10 sr at 550 nm for haze aerosols from four AERONET sites located in East Asia: Anmyeon and Jeju in Korea, Chen-Kung in Taiwan, and Beijing in China. The lidar-ratio values (58.2 ± 3.8 sr at 532 nm) of anthropogenic aerosols obtained in this study are similar to or slightly higher than those of East-Asian haze aerosols generated from fossil fuel consumption and domestic biomass burning (Ansmann et al., 2005; Cattrall et al., 2005).

It was assumed that aerosols transported from the north through Korea must have been strongly affected by forest-fire smoke that was originated from eastern Siberia areas. That conclusion follows from the specific spectral behaviors of lidar ratios at 355 and 532 nm and the origin of the air masses. Müller et al. (2005) found that mean lidar ratios of aged forest-fire smoke were lower at 355 nm than at 532 nm. A similar spectral behavior was found from multi-wavelength Raman lidar observations of Siberian forest-fire smoke detected over Tokyo, Japan (Murayama et al., 2004) and of biomass-burning aerosols advected from Canada to Germany (Wandinger et al., 2002). Differences between the lidar ratios observed at 355 nm and 532 nm in this study were smaller than those reported by Müller et al. (2005) (37.9 ± 13.1 sr at 355 nm and 52.3 ± 16.6 sr at 532 nm) and by Murayama et al. (2004) ($\sim$40 sr at 355 nm and $\sim$65 sr at 532 nm). Note that the forest-fire smoke plumes studied by Murayama et al. (2004) were detected in the free troposphere while our observations were measured within the PBL. Noh et al. (2007) reported a similar spectral behavior of the lidar ratio within the PBL over Anmyeon Island for air masses transported from the Siberian region. Although the aerosol layers listed in Table 1 were likely affected by local sources at low observation heights, it is believed that their optical properties were still mainly influenced by the forest-fire smoke.

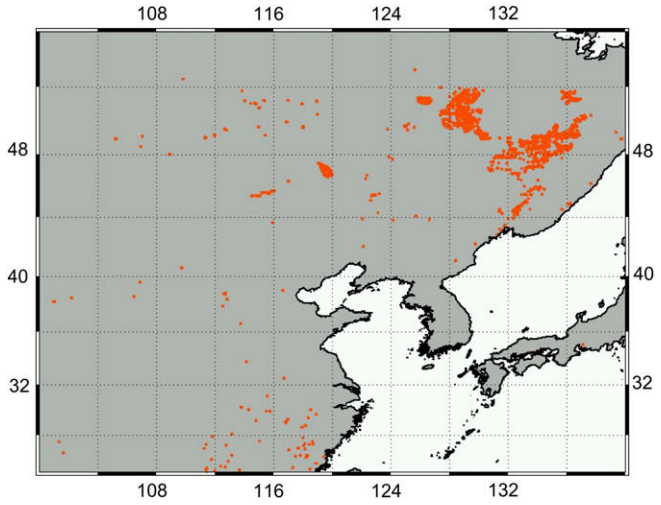

Fig. 6. MODIS active fire products (MOD14) for the period of October 17–27, 2005. The total number of fires was 4045.

The average Ångström exponents for anthropogenic and smoke aerosols are 0.87 and 0.92, respectively. These values are comparable to those found for pollution outbreaks in the northeast Asian region (Ansmann et al., 2005; Cattrall et al., 2005). The low Ångström exponent values seem to be closely related to the higher hygroscopic growth factor (f(RH)) of pollution aerosols from China under high relative humidity. The mean f(RH) during the observation periods was 1.90 ± 0.27, which is higher than that of European anthropogenic aerosols observed during ACE-2 (1.46 ± 0.10; Carrico et al., 2000) and of smoke aerosols in northeast Asia (1.60 ± 0.20; Kim et al., 2006a). However, it is lower than that reported for pollution aerosol directly transported from China to Gosan, Korea (2.75 ± 0.38; Kim et al., 2006a,b). Forest-fire smoke particles can grow during long-range transport in the free troposphere (Müller et al., 2007). It can be assumed that the low Ångström exponent value of smoke aerosols found in this study was strongly affected by high relative humidity conditions rather than transport time.

Table 2 summarizes the microphysical parameters derived from the inversion of the lidar data of each aerosol layer, including particle effective radius, complex refractive index, and single-scattering albedo. Inversion results for the October 18 measurements were not available due to the lack of 1064-nm lidar data. For comparison purposes, results obtained in the East Asia region by

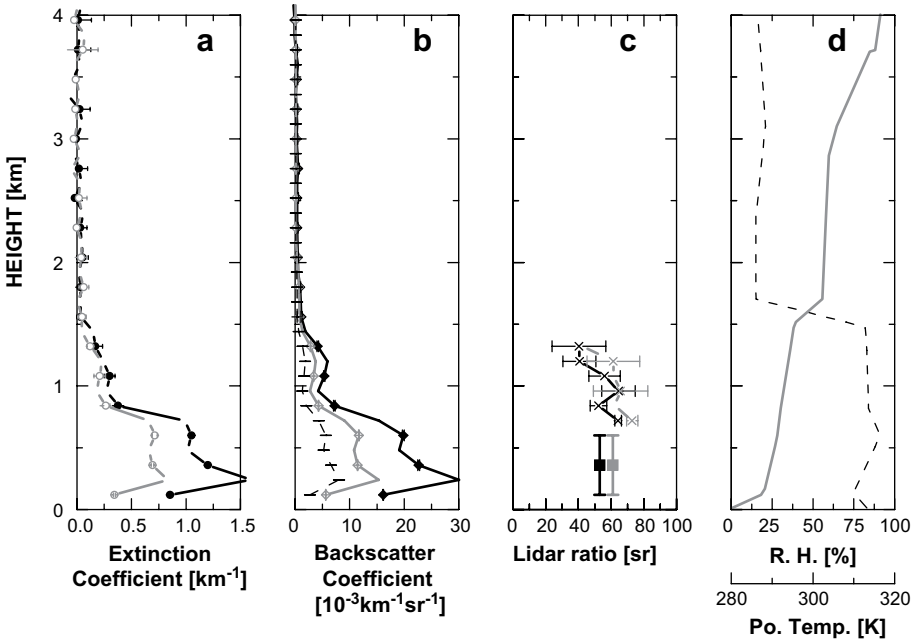

Fig. 7. Raman lidar analysis and radiosonde results obtain on October 24, 2005. (a) Extinction coefficients at 355 (black) and 532 (gray) nm, (b) backscatter coefficients at 355 (black), 532 (gray), and 1064 (black dotted) nm, and (c) lidar ratios at 355 (black) and 532 (gray) nm. Below 780 m altitude denote average values estimated for the boundary layer. (d) Relative humidity (dotted line) and potential temperature (gray line) measured by radiosonde.

others are included in Table 3. Effective radii obtained in this study (0.32–0.36 μm) are considerably larger than those from the Pearl River Delta (0.24 ± 0.07 μm) and Beijing (0.23 ± 0.06 μm) areas (Müller et al., 2006). Forest-fire smoke transported from Siberia to Tokyo, Japan also showed a lower value (0.22 ± 0.04 μm; Murayama et al., 2004). The relatively large effective radii obtained in this study can be explained by hygroscopic growth under high relative humidity conditions.

The mean values of the real part of the refractive index are 1.44 ± 0.01 and 1.41 ± 0.01 for anthropogenic aerosols and smoke aerosols, respectively, which are lower than those of urban haze particles observed in the Pearl River Delta (1.57 ± 0.11), and in Beijing (1.62 ± 0.11) (Müller et al., 2006). Müller et al. (2005) reported real parts of the refractive index of 1.47 ± 0.07 for forest-fire smoke particles and 1.52 ± 0.01 for pollution particles advected from North America to Leipzig (51.3°N, 12.4°E), Germany. In many cases, the anthropogenic pollution particles have higher real parts of the refractive index than particles from forest-fire smoke. The real part of the refractive index obtained in this study is even smaller than those reported by Müller et al. (2005). These lower values and the higher effective radii obtained in this study might be due to high relative humidity conditions. Such an impact is negligible in the case of the observations by Müller et al. (2005) who observed particles in the free troposphere.

In contrast to the results for the real part of the refractive index, the imaginary part of the refractive index and the single-scattering albedo were quite different between anthropogenic aerosol and smoke aerosol. The mean imaginary part of the refractive index of anthropogenic aerosols is 0.010 ± 0.001, which is higher than that of smoke aerosols (0.006 ± 0.001). Müller et al. (2006) found even higher imaginary parts of the refractive index for aerosols in the Pearl River Delta (South China) and in Beijing (North China), namely, 0.022 ± 0.015 and 0.019 ± 0.012, respectively. In this study, a moderately low single-scattering albedo value (0.96 ± 0.02) was obtained for smoke aerosols, while even lower values (0.90 ± 0.03)

Table 1
Average values of lidar ratio (S_a), Ångström exponent (Å), and relative humidity (RH) measured for the observed aerosol layers.

October, 2005		Height (km)	S_a (sr)[a]		Å[b]	RH[c] (%)
			532 nm	355 nm		
Anthropogenic aerosol	15th	0.78–1.38	56 ± 8	53 ± 6	0.92	66–79
	17th	0.78–1.38	53 ± 17	55 ± 9	0.95	62–88
	18th	0.78–1.62	63 ± 9	59 ± 3	0.98	55–69
	23rd	0.78–1.38	61 ± 8	55 ± 6	0.60	65–89
	24th	0.78–1.26	59 ± 15	58 ± 14	0.90	83–91
Average			59 ± 10	56 ± 7	0.87	
Smoke aerosol	19th	0.78–1.62	64 ± 7	54 ± 7	0.90	85–91
	26th	0.78–1.50	63 ± 10	56 ± 10	0.83	50–88
	27th	0.78–1.38	62 ± 5	57 ± 6	1.02	49–88
Average			63 ± 7	56 ± 7	0.92	

[a] Lidar ratio.
[b] Ångström exponent.
[c] Relative humidity.

Table 2
Microphysical parameters derived from the inversion of lidar data.

October, 2005		γ_{eff}[a]	Refractive index		SSA[d]
			m_{real}[b]	m_{Image}[c]	
Anthropogenic aerosol (west)	15th	0.36 ± 0.03	1.43 ± 0.03	0.008 ± 0.006	0.93 ± 0.02
	17th	0.35 ± 0.02	1.45 ± 0.04	0.009 ± 0.005	0.89 ± 0.01
	23rd	0.34 ± 0.03	1.45 ± 0.05	0.012 ± 0.007	0.87 ± 0.02
	24th	0.33 ± 0.03	1.43 ± 0.04	0.010 ± 0.004	0.92 ± 0.01
Average		0.35 ± 0.01	1.44 ± 0.04	0.010 ± 0.006	0.90 ± 0.03
Smoke aerosol (north)	19th	0.34 ± 0.03	1.41 ± 0.02	0.005 ± 0.002	0.97 ± 0.01
	26th	0.35 ± 0.04	1.42 ± 0.03	0.007 ± 0.003	0.94 ± 0.01
	27th	0.32 ± 0.01	1.40 ± 0.03	0.005 ± 0.003	0.97 ± 0.00
Average		0.33 ± 0.02	1.41 ± 0.03	0.006 ± 0.003	0.96 ± 0.02

[a] Effective radius.
[b] Real part of refractive index.
[c] Imaginary part of refractive index.
[d] Single-scattering albedo.

Table 3
Particle effective radius, real and imaginary parts of the refractive index, and single-scattering albedo for different aerosol types.

Aerosol type	Source region	γ_{eff}	Refractive index		SSA	Reference
			m_{real}	m_{Image}		
Anthropogenic aerosol	Northeast China	0.35 ± 0.01	1.44 ± 0.03	0.010 ± 0.006	0.90 ± 0.03	In this study
Smoke aerosol	The Maritime Province of Siberia	0.33 ± 0.02	1.41 ± 0.03	0.006 ± 0.003	0.96 ± 0.02	In this study
Forest-fire smoke	East/Central Siberia and central Canada	0.36 ± 0.05	1.46 ± 0.07	0.003 ± 0.003	0.93 ± 0.03	Müller et al. (2005)
Forest-fire smoke	Siberia	0.22 ± 0.04	–	–	0.95 ± 0.06	Murayama et al. (2004)
Haze plume	North America	0.17 ± 0.02	1.52 ± 0.01	0.002 ± 0.001	–	Müller et al. (2005)
Urban haze	South China	0.24 ± 0.07	1.57 ± 0.11	0.022 ± 0.015	0.77 ± 0.12	Müller et al. (2006)
Urban haze	North China	0.23 ± 0.06	1.62 ± 0.11	0.019 ± 0.012	0.78 ± 0.11	Müller et al. (2006)
Smoke plume	Mexico		1.41–1.45		0.97	Kredenweis et al. (2001)[a]

[a] Values were measured at 670 nm by sunphotometer.

were obtained for anthropogenic aerosols. Light-absorption characteristics of anthropogenic aerosols observed in this study are comparable to that of pollution particles observed in urban areas of China (Qiu et al., 2004; Eck et al., 2005) with single-scattering albedos (SSA) at 550 nm of 0.82–0.87 (Qiu et al., 2004) and 0.88 (Eck et al., 2005) at Beijing. Lee et al. (2006a,b) found a SSA of 0.88 for haze particles transported from large urban areas in China to the Korean peninsula.

In this study, the SSA of smoke aerosols was slightly higher than that of anthropogenic aerosols. It was reported that the single-scattering albedo of the Siberian forest-fire plume observed with a Raman lidar over Tokyo, Japan (Murayama et al., 2004) and over Leipzig, Germany (Müller et al., 2005) was 0.95 ± 0.06 and 0.93 ± 0.03, respectively, which are similar to those observed in this study. A high single-scattering albedo of ~0.97 at 670 nm was reported for aged biomass-burning plumes advected from Mexico to the United States, which was influenced by water uptake of the particles during the transport (Kredenweis et al., 2001). Related to distance of transport, Ferrare et al. (1990) estimated an increase of single-scattering albedo of smoke from boreal-forest fires with distance from the fire sources based on satellite observations. Colarco et al. (2004) measured single-scattering albedos of 0.93 ± 0.02 at 550 nm for smoke aerosol from boreal fires over central Quebec 1000 km downwind of the source region in the summer of 2002.

The observed differences in the light-absorption characteristics between the two types of aerosol result from the differences in source region and chemical composition. Fig. 8 shows the temporal variations of the organic carbon (OC), elemental carbon (EC), and OC/EC ratio. A high OC/EC ratio was observed during the smoke aerosol periods of October 19, 20, 26, and 27, 2005. Aerosols originated from China contained a high amount of light-absorbing black carbon from industrial emissions and the combustion of biomass and fossil fuels. Table 4 summarizes the characteristics of the OC, EC, and OC/EC ratios for the different emission sources and regions. OC/EC ratios for aerosols from coal combustion and motor vehicle in China show lower values than those from wood burning and forest fires. Coal combustion and motor vehicles emissions are the main sources of pollution in urban areas in China. The mean OC/EC ratio of anthropogenic aerosols (2.5 ± 0.4) observed in this study is similar to that of urban aerosols in China; 2.5 ± 0.4 (Ye et al., 2003). The mean OC/EC ratio of smoke aerosols observed in this study, 4.1 ± 0.5, is clearly distinguishable from that of anthropogenic aerosols and is smaller than that of forest-fire smoke particles observed in Colorado, USA. In Korea, open field burning of agricultural waste after the harvest of rice is commonly practiced in fall (Ryu et al., 2004). Considering observation periods and the altitudes of the observed layers (within the PBL) it can be concluded that the aerosol composition was largely affected by such open field burning. The OC/EC ratios of anthropogenic aerosols are clearly distinguishable from those of biomass-burning and/or forest-fire smoke. It can be concluded that aerosols from China consist of highly light-absorbing particles.

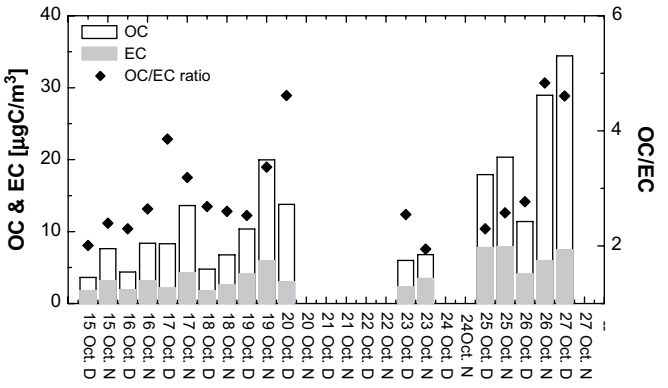

Fig. 8. OC and EC, and the OC-to-EC ratios measured during the observation period.

Table 4
OC, EC, and OC-to-EC ratio observed in different regions.

Region	Major emission source	OC ($\mu g\,m^{-3}$)	EC ($\mu g\,m^{-3}$)	OC/EC ratio	References
Shanghai, China[a]	Coal combustion	28.5	11.5	2.5	Ye et al. (2003)
Hong Kong, China[b]	Motor vehicle	5.3 ± 2.1	3.2 ± 2.6	1.9	Cao et al. (2004)
Gwangzhou, China[b]	Motor vehicle	15.8 ± 6.4	5.9 ± 2.1	2.7	Cao et al. (2004)
Shenzhen, China[b]	Motor vehicle	7.6 ± 4.9	4.2 ± 3.1	1.8	Cao et al. (2004)
Zhuhai, China[b]	Motor vehicle	5.4 ± 3.4	1.9 ± 0.9	2.9	Cao et al. (2004)
PRDR,[c] China[b]	Motor vehicle	9.2 ± 6.5	4.1 ± 2.7	2.5	Cao et al. (2004)
Beijing, China[b]	Coal consumption	28.79	10.23	2.8	He et al. (2001)
Colorado, USA[b]	Residential wood combustion	51.4 ± 11.7	12.4 ± 4.2	4.2	Watson et al. (2001)
Colorado, USA[b]	Forest fire	46.9 ± 15.7	3.2 ± 1.8	14.5	Watson et al. (2001)
Gwangju, Korea[b]	Post-harvest of barley	21.6 ± 8.2	2.9 ± 0.7	7.3	Ryu et al. (2004)
Gwangju, Korea[b]	Post-harvest of rice	20.5 ± 8.7	2.6 ± 1	8.3	Ryu et al. (2004)
Gwangju, Korea[b]	Anthropogenic aerosol	13.4 ± 9.1	5.4 ± 3.2	2.5	
Gwangju, Korea[b]	Smoke aerosol	26.0 ± 6.8	6.3 ± 2.0	4.1	This study

[a] Mass % of fine particle mass.
[b] Mass concentration ($\mu g\,m^{-3}$).
[c] Pearl River Delta Region.

4. Conclusion

Integrated monitoring of atmospheric aerosol was performed using satellite, ground-based sunphotometer, semi-real-time carbon particle analyzer, and a multi-wavelength Raman lidar data in Gwangju, Korea from October 15 to 28, 2005. High aerosol mass concentrations were measured during two haze periods (October 17–20, 2005 and October 24–28, 2005) and the maximum value of 159 $\mu g\,m^{-3}$ was reached on October 25, 2005, as was the highest AOD value (2.28 at 440 nm). According to the air mass movement patterns based on HYSPLIT backward trajectory calculations, the greatest differences in optical and microphysical parameters retrieved from multi-wavelength Raman lidar observations were found in light-absorbing properties such as the imaginary part of the refractive index and single-scattering albedo.

The aerosols transported to Korea from China on October 15, 17, 23–24 showed moderate light-absorbing characteristics with an average imaginary part of the refractive index of 0.010 ± 0.002 and a single-scattering albedo of 0.90 ± 0.03. The aerosols transported from East Siberia on October 19, and 26–27 showed low light-absorbing characteristics with an imaginary part of the refractive index of 0.006 ± 0.001 and a single-scattering albedo of 0.96 ± 0.02. The OC/EC ratio obtained by semi-real-time in-situ carbon particle analyzer also indicated the differences depending on air mass movement patterns.

The approach of integrated monitoring of aerosol plumes with the use of satellite data, sunphotometer data, in-situ instruments, and multi-wavelength Raman lidar data allows us to determine aerosol optical and microphysical characteristics and source origins. The integrated monitoring approach described in this study permits us to gain more insight into the mechanisms of long-range transport of pollution, and the impact of such pollution on air quality in Korea. Furthermore, it provides us more information on the light-absorbing characteristics, as well as the vertical distribution of haze layers during long-range transport, which are needed for better assessment of the effect of atmospheric aerosols on radiative forcing and further climate change.

Acknowledgement

This work was supported by the Korea Meteorological Administration Research and Development Program under Grant CATER 2007-4108. This research was partially supported by the Brain Korea 21(BK21) program for the fellowship of Young M. Noh. The authors would like to thank GSFC/NASA for the use of AERONET sunphotometer data.

References

Ansmann, A., Wandinger, U., Riebesell, M., Weitkamp, C., Michaelis, W., 1990. Measurement of atmospheric aerosol extinction profiles with a Raman lidar. Optics Letters 15, 746–748.

Ansmann, A., Wandinger, U., Riebesell, M., Weitkamp, C., Michaelis, W., 1992. Independent measurement of extinction and backscatter profiles in cirrus clouds by using a combined Raman elastic-backscatter lidar. Applied Optics 31, 7113–7131.

Ansmann, A., Althausen, D., Wandinger, U., Franke, K., Müller, D., Wagner, F., Heintzenberg, J., 2000. Vertical profiling of the Indian aerosol plume with six-wavelength lidar during INDOEX: a first case study. Geophysical Research Letters 27, 963–966.

Ansmann, A., Engelmann, R., Althausen, D., Wandinger, U., Hu, M.m, Zhang, Y., 2005. High aerosol load over Pearl River Delta, China, observed with Raman lidar and Sun photometer. Geophysical Research Letters 32, L13815.

Arimoto, R., Kim, Y.J., Kim, Y.P., Quinn, P.K., Bates, T.S., Anderson, T.L., Gong, S., Uno, I., Chin, M., Huebert, B.J., Clarke, A.D., Shinozuka, Y., Weber, R.J., Anderson, J.R., Guazzotti, S.A., Sullivan, R.C., Sodeman, D.A., Prather, K.A., Sokolik, I.N., 2006. Characterization of Asian dust during ACE-Asia. Global and Planetary Change 52, 23–56.

Bohren, C.F., Huffman, D.R., 1983. Absorption and Scattering of Light by Small Particles. John Wiley, New York, p. 530.

Cao, J.J., Lee, S.C., Ho, K.F., Zou, S.C., Fung, K., Li, Y., Watson, J.G., Chow, J.C., 2004. Spatial and seasonal variations of atmospheric organic carbon and elemental carbon in Pearl River Delta Region, China. Atmospheric Environment 38, 4447–4456.

Carrico, C.M., Rood, M.J., Ogren, J.A., Neusü, X.C., Wiedensohler, A., Heintzenberg, J., 2000. Aerosol optical properties at Sagres, Portugal during ACE-2. Tellus-B 52B, 694–715.

Cattrall, C., Reagan, J., Thome, K., Dubovik, O., 2005. Variability of aerosol and spectral lidar and backscatter and extinction ratios key aerosol types derived from selected Aerosol Robotic Network locations. Journal of Geophysical Research 110, D10S11. doi:10.1029/2004JD005124.

Colarco, P.R., Schoeberl, M.R., Doddridge, B.G., Marufu, L.T., Torres, O., Welton, E.J., 2004. Transport of smoke from Canadian forest fires to the surface near Washington, D.C.: injection height, entrainment, and optical properties. Journal of Geophysical Research 109, D06203. doi:10.1029/2003JD004248.

Chun, Y., Park, S., Boo, K., Kim, J., Lee, M., 2001. Synopsis, transport, and physical characteristics of Asian dust in Korea. Journal of Geophysical Research 106 (D16), 18067–18074.

Draxler, R.R., Rolph, G.D., 2003. HYSPLIT (HYbrid Single-Particle Lagrangian Integrated Trajectory) Model Access via NOAA ARL READY. NOAA Air Resources Laboratory, Silver Spring, MD. Available from: <http://www.arl.noaa.gov/ready/hysplit4.htmlS>.

Dubovik, O., King, M.D., 2000. A flexible inversion algorithm for retrieval of aerosol optical properties from sun and sky radiance measurements. Journal of Geophysical Research 105 (D16), 20673–20696.

Dubovik, O., Holben, B.N., Lapyonok, T., Sinyuk, A., Mishchenko, M.I., Yang, P., Slutsker, I., 2002. Non-spherical aerosol retrieval method employing light scattering by spheroids. Geophysical Research Letters 29, 54-1–54-4.

Eck, T.F., Holben, B.N., Dubovik, O., Smirnov, A., Goloub, P., Chen, H.B., Chatenet, B., Gomes, L., Zhang, X.-Y., Tsay, S.-C., Ji, Q., Giles, D., Slutsker, I., 2005. Columnar aerosol optical properties at AERONET sites in central eastern Asia and aerosol transport to the tropical mid-Pacific. Journal of Geophysical Research 110, D06202. doi:10.1029/2004JD005274.

Ferrare, R.A., Fraser, R.S., Kaufmann, Y.J., 1990. Satellite measurements of large-scale air pollution: measurements of forest fire smoke. Journal of Geophysical Research 95, 9911–9925.

Ferrare, R.A., Turner, D.D., Brasseur, L.H., Feltz, W.F., Dubovik, O., Tooman, T.P., 2001. Raman lidar measurements of the aerosol extinction-to-backscatter ratio over the Southern Great Plains. Journal of Geophysical Research 106, 20333–20347.

He, K., Yang, F., Ma, Y., Zhang, Q., Yao, X., Chan, C.K., Cadle, S., Chan, T., Mulawa, P., 2001. The characteristics of PM2.5 in Beijing, China. Atmospheric Environment 35, 4959–4970.

Huebert, B.J., Bates, T., Russell, P.B., Shi, G., Kim, Y.J., Kawamura, K., Carmichael, G., Nakajima, T., 2003. An overview of ACE-Asia: strategies for quantifying the relationships between Asian aerosols and their climatic impacts. Journal of Geophysical Research 108 (D23), 8633.

IMPROVE, 2000. Spatial and Seasonal Patterns and Temporal Variability of Haze and its Constituents in the United States: Report III Available from: <http://vista.cira.colostate.edu/improve/Publications/Reports/2000/2000.htm>.

Kaufman, Y.J., Justice, C.O., Flynn, L.P., Kendall, J.D., Prins, E.M., Giglio, L., Ward, D.E., Menzel, P., Setzer, A.W., 1998. Potential global fire monitoring from EOS-MODIS. Journal of Geophysical Research 103, 31955–32215.

Kim, J.Y., Yoon, S.C., Jefferson, A., Kim, S.W., 2006a. Aerosol hygroscopic properties during Asian dust, pollution, and biomass burning episodes at Gosan, Korea in April 2001. Atmospheric Environment 40, 1550–1560.

Kim, Y.J., Kim, M.J., Lee, K.H., Park, S.S., 2006b. Investigation of carbon pollution episodes using semicontinuous instrument in Incheon, Korea. Atmospheric Environment 40, 4064–4075.

Kim, K.W., He, Z., Kim, Y.J., 2004. Physico-chemical characteristics and radiative properties of Asian dust particles observed at Kwangju, Korea during the 2001 ACE-Asia IOP. Journal of Geophysical Research 109 (D19). doi:10.1029/2003JD003693.

Kim, K.W., 2007. Physico-chemical characteristics of visibility impairment by airborne pollen in an Urban Area. Atmospheric Environment. doi:10.1016/j.atmosenv.2006.12.054.

Kredenweis, S.M., Remer, L.A., Bruintjes, R., Dubovik, O., 2001. Smoke aerosol from biomass burning in Mexico: hygroscopic smoke optical model. Journal of Geophysical Research 106 (5), 4831–4844.

Lee, K.H., Kim, J.E., Kim, Y.J., Kim, J., Hoyningen-Huene, W., 2005. Impact of the smoke aerosol from Russian forest fires on the atmospheric environment over Korea during May 2003. Atmospheric Environment 39, 58–99.

Lee, K.H., Kim, Y.J., Kim, M.J., 2006a. Characteristics of aerosol observed during two severe haze events over Korea in June and October 2004. Atmospheric Environment 40, 5146–5155.

Lee, K.H., Kim, Y.J., von Hoyningen-Huene, W., Burrow, J.P., 2006b. Influence of land surface effects on MODIS aerosol retrieval using BAER method over Korea. International Journal of Remote Sensing of Environment 27 (12–14), 2813–2830.

Lee, K.H., Kim, Y.J., von Hoyningen-Huene, W., Burrow, J.P., 2007. Spatio-temporal variability of satellite-derived aerosol optical thickness over northeast Asia in 2004. Atmospheric Environment. doi:10.1016/j.atmosenv.2007.01.048.

Luo, Y., Lu, D., Zhou, X., Li, W., 2001. Characteristics of the spatial distribution and yearly variation of aerosol optical depth over China in last 30 years. Journal of Geophysical Research 106, 14501–14513.

Matthias, V., Balis, D., Bosenberg, J., Eixmann, R., Iarlori, M., Komguem, L., Mattis, I., Papayannis, A., 2004. Vertical aerosol distribution over Europe: statistical analysis of Raman lidar data from 10 European Aerosol Research Lidar Network

(EARLINET) stations (DOI 10.1029/2004JD004638). Journal of Geophysical Research 109 (18), D18201.
Molena, J.V., 1997. Analysis of the real world performance of the Optec NGN-2 ambient nephelometer. In: Proceedings of Visual Air Quality, Aerosols, and Global Radiation Balance. Air & Waste Management Association, Pittsburgh, PA, pp. 243–265.
Müller, D., Wandinger, U., Ansmann, A., 1999a. Microphysical particle parameters from extinction and backscatter lidar data by inversion with regularization: theory. Applied Optics 38, 2346–2357.
Müller, D., Wandinger, U., Ansmann, A., 1999b. Microphysical particle parameters from extinction and backscatter lidar data by inversion with regularization: simulation. Applied Optics 38, 2358–2368.
Müller, D., Wagner, F., Wandinger, U., Ansmann, A., Wendisch, M., Althausen, D., von Hoyningen-Huene, W., 2000a. Microphysical particle parameters from extinction and backscatter lidar data by inversion with regularization: experiment. Applied Optics 39, 1879–1892.
Müller, D., Wagner, F., Althausen, D., Wandinger, U., Ansmann, A., 2000b. Physical particle properties of the Indian aerosol plume derived from six-wavelength lidar observations on 25 March 1999 of the Indian Ocean Experiment. Geophysical Research Letters 27, 1403–1406.
Müller, D., Franke, K., Ansmann, A., Althausen, D., 2003. Indo-Asian pollution during INDOEX: microphysical particle properties and single-scattering albedo inferred from multiwavelength lidar observations. Journal of Geophysical Research 108, 4600. doi:10.1029/2003JD003538.
Müller, D., Mattis, I., Wandinger, U., Ansmann, A., Althausen, D., Stohl, A., 2005. Raman lidar observations of aged Siberian and Canadian forest fire smoke in the free troposphere over Germany in 2003: microphysical particle characterization. Journal of Geophysical Research, D17201. doi:10.1029/2004JD005756.
Müller, D., Tesche, M., Eichler, H., Engelmann, R., Althausen, D., Ansmann, A., Cheng, Y.F., Zhang, Y.H., Hu, M., 2006. Strong particle light-absorption over the Pearl River Delta (South China) and Beijing (North China) determined from combined Raman lidar and Sun photometer observations. Geophysical Research Letters 33, L20811. doi:10.1029/2006GL027196.
Müller, D., Ansmann, A., Mattis, I., Tesche, M., Wandinger, U., Althausen, D., Pisani, G., 2007. Aerosol-type-dependent lidar ratios observed with Raman lidar. Journal of Geophysical Research 112 (D16). doi:10.1029/2006JD008292.
Murayama, T., et al., 2003. An intercomparison of lidar-derived aerosol optical properties with airborne measurements near Tokyo during ACE-Asia. Journal of Geophysical Research 108, 8651. doi:10.1029/2002JD003259.
Murayama, T., Müller, D., Wada, K., Shimizu, A., Sekiguchi, M., Tsukamoto, T., 2004. Characterization of Asian dust and Siberian smoke with multi-wavelength Raman lidar over Tokyo, Japan in spring 2003. Geophysical Research Letter 31, L23103.
Noh, Y.M., Kim, Y.J., Choi, B.C., Murayama, T., 2007. Aerosol lidar ratio characteristics measured by a multi-wavelength Raman lidar system at Anmyeon Island, Korea. Atmospheric Research. doi:10.1016/j.atmosres.2007.03.006.
Noh, Y.M., Kim, Y.J., Müller, D., 2008. Seasonal characteristics of lidar ratio measured with a Raman lidar at Gwangju, Korea in spring and autumn. Atmospheric Environment 42, 2208–2224.
Park, S.S., Kim, Y.J., 2004. PM2.5 particles and size-segregated ionic species measured during fall season in three urban sites in Korea. Atmospheric Environment 38 (10), 1459–1471.
Qiu, J., Yang, L., Zhang, X., 2004. Characteristics of the imaginary part and single-scattering albedo of urban aerosols in northern China. Tellus, Series B 56, 276–284.
Ricchiazzi, P., Yang, S., Gautier, C., Sowle, D., 1998. SBDART: a research and teaching software tool for plane-parallel radiative transfer in the earth's atmosphere. Bulletin of the American Meteorological Society 79 (10), 2101–2114.
Ryan, A.R., Lowenthal, D., Kumar, N., 2005. Improved light extinction reconstruction in interagency monitoring of protected visual environments. Journal of the Air & Waste Management Association 55, 1751–1759.
Ryu, S.Y., Kim, J.E., Zhuanshi, H., Kim, Y.J., 2004. Chemical composition of post-harvest biomass burning aerosols in Gwangju, Korea. Journal of the Air & Waste Management Association 54 (9), 1124–1137.
Tesche, M., Ansmann, A., Müller, D., Althausen, D., Engelmann, R., Hu, M., Zhang, Y., 2007. Particle backscatter, extinction, and lidar ratio profiling with Raman lidar in south and north China. Applied Optics 46, 6302–6308.
Veselovskii, I., Kolgotin, A., Griaznov, V., Müller, D., Wandinger, U., Whiteman, D.N., 2002. Inversion with regularization for the retrieval of tropospheric aerosol parameters from multiwavelength lidar sounding. Applied Optics 41, 3685–3699.
von Hoyningen-Huene, W., Freitag, M., Burrows, J.B., 2003. Retrieval of aerosol optical thickness over land surfaces from top-of-atmosphere radiance. Journal of Geophysical Research 108 (D9), 4260.
Wandinger, U., Ansmann, A., Reichardt, J., Deshler, T., 1995. Determination of stratospheric aerosol microphysical properties from independent extinction and backscattering measurements with a Raman lidar. Applied Optics 34, 8315–8329.
Wandinger, U., Ansmann, A., 2002. Experimental determination of the lidar overlap profile with Raman lidar. Applied Optics 41 (3), 511–514.
Wandinger, U., Müller, D., Bockmann, C., Althausen, D., Matthias, V., Bösenberg, J., Weiß, V., Fiebig, M., Wendisch, M., Stohl, A., Ansmann, A., 2002. Optical and microphysical characterization of biomass burning and industrial pollution aerosols from multiwavelength lidar and aircraft measurements. Journal of Geophysical Research 107, 8125. doi:10.1029/2000JD000202.
Watson, J.G., Chow, J.C., Houck, J.E., 2001. PM2.5 chemical source profiles for vehicle exhaust, vegetative burning, geological material, and coal burning in Northwestern Colorado during 1995. Chemosphere 43, 1141–1151.
Ye, B., Ji, X., Yang, H., Yao, X., Chan, C.K., Cadle, S.H., Chan, T., Mulawa, P.A., 2003. Concentration and chemical composition of PM2.5 in Shanghai for a 1-year period. Atmospheric Environment 37, 499–510.